Plasma Physics and
Controlled Fusion

PAPER • **OPEN ACCESS**

Motional Stark Effect measurements and modelling at Wendelstein 7-X

To cite this article: M Zanini *et al* 2026 *Plasma Phys. Control. Fusion* **68** 065033

Plasma Physics and Controlled Fusion

OPEN ACCESS

RECEIVED
30 January 2026

REVISED
16 May 2026

ACCEPTED FOR PUBLICATION
2 June 2026

PUBLISHED
16 June 2026

PAPER

Motional Stark Effect measurements and modelling at Wendelstein 7-X

M Zanini[1,*], O Ford[1], S Bannmann[1], E V Hausten[1], J Kügler[1], P Zs Poloskei[1], K Rahbarnia[1], T Romba[1], R C Wolf[1,2] and W7-XTeam[3]

[1] Max-Planck-Institut für Plasmaphysik, 17491 Greifswald, Germany
[2] Institut für Physik und Astronomie, Technische Universität Berlin, 10623 Berlin, Germany
[3] See Grulke *et al* 2024 http://dx.doi.org/10.1088/1741-4326/ad2f4d for the W7-X team.
[*] Author to whom any correspondence should be addressed.

E-mail: marco.zanini@ipp.mpg.de

Keywords: stellarator, motional stark effect, spectroscopy

Abstract

The motional stark effect (MSE) is an effective method to assess the rotational transform in magnetic confined plasmas by measuring the polarisation angle of the emitted light. It relies on the Stark-splitting of the Balmer alpha emission, caused by the interaction between the injection of neutral beams and the background plasma. A prototype MSE diagnostic system, which relies on spectrum measurements taken using different linear polarising filters, has been installed on the Wendelstein 7-X stellarator (W7-X), and its diagnostic capabilities have been demonstrated. In this work we present an upgraded MSE diagnostic system and discuss the comparison between the experimental data and the forward model originally developed for the beam emission spectroscopy measurements at W7-X and modified to include the polarising optical elements. The experimental data and the model results show a good agreement for relative changes of the polarisation angle for different plasma β. However, the evolution of the polarisation angle during electron cyclotron current drive experiments could not yet be resolved due to limited signal-to-noise ratio. Possible upgrades to improve diagnostic performance are outlined.

1. Introduction

The control of the rotational transform in a Stellarator is a key element for ensuring high plasma performance [1]. Additionally, since Wendelstein 7-X (W7-X) is a low shear device [2, 3], even small changes of the rotational transform profile can have significant effects, as it was seen during electron cyclotron current drive [4] (ECCD) experiments. During these experiments the local rotational transform changes made by localised currents made the plasma unstable, resulting in sawtooth-like crashes [5, 6]. Although the rotational transform is a crucial parameter, W7-X currently lacks a routine method for its inference. Establishing such a capability would enhance experimental understanding and strengthen code validation and equilibrium reconstruction.

The rotational transform can be assessed by a motional stark effect (MSE) diagnostic [7, 8], which relies on the polarisation of the Stark split emission of neutral beam injected particles, created by an electric field $\mathbf{E} = \mathbf{v} \times \mathbf{B}$, where $\mathbf{v}$ is the beam velocity and $\mathbf{B}$ the magnetic field. The spectrum consists of $\sigma\,(\Delta m \pm 1)$ and $\pi\,(\Delta m = 0)$ components (with m being the magnetic quantum number), each one composed of three transitions whose polarisation depends on $\mathbf{E}$. If the line of sight (LOS) is purely transverse to the electric field, the π and σ emission are linearly polarised parallel and perpendicular to $\mathbf{E}$, respectively. Instead, for a line of sight purely parallel to $\mathbf{E}$, the π line emission is not observed, whereas the σ line is characterised by an overlap of left and right circular polarisation, which cancels out and results in unpolarised emission. The MSE diagnostic is therefore used to measure the light polarisation, from which the direction of $\mathbf{E}$, and therefore $\mathbf{B}$ can be obtained. From the magnetic field direction, the rotational transform can in principle be inferred. Since, in a stellarator, the rotational transform

exists even in vacuum, an MSE diagnostic in such a device offers the attractive feature of not requiring an absolute measurement of the light polarisation; in principle, relative measurements with respect to the vacuum should suffice to determine it. On the other hand, as a stellarator presents a fully 3D magnetic field and the minimisation of the toroidal current is one of the optimisation criteria of W7-X, a high measurement sensitivity is required. A previously installed MSE prototype [9] demonstrated the diagnostic capabilities of such a system at W7-X, however due to the low signal-to-noise ratio (SNR which scales as $\sqrt{N}$, where N is the photon number) it was not suited for in-depth physics studies. An upgraded diagnostic, with larger optical fibres and a higher throughput spectrometer was installed and is discussed in this work. In chapter 2 we will discuss the diagnostic hardware, in chapter 3 the Stokes notation, which is used to infer the light polarisation (chapter 4). In chapter 5 we discuss the expected results obtained by a forward model for realistic plasma pressures and currents whereas in chapter 6 we discuss the results for a representative experiment and compare them with the modelled data, demonstrating a generally good match between the experimental observations and the model predictions. Finally, in section 7 we discuss further hardware improvements and the perspective of the diagnostic at W7-X. The scope of this paper is to present the upgraded system and demonstrate its capability to measure relative changes in the polarisation angle that are broadly consistent with the predictions of the forward model for a representative experiment. While overall agreement between model and experiment is observed, some discrepancies remain and will require further investigation. An in-depth analysis, as well as the demonstration of the system's applicability to equilibrium reconstruction, is left for future work.

2. Diagnostic hardware

The MSE diagnostic is composed of an optical head with optical elements, transfer fibres, a spectrometer and a sCMOS camera. The MSE optical head is mounted on the charge exchange recombination spectroscopy (CXRS) system [10] (see figure 1) and consists in a 2D grid (13×4) of optical fibres (400 μm, 40 μm cladding, NA$=0.22$). In the reference CXRS publication ([10]) the interested reader can find more details and information regarding the hardware components and optics. The head is covered by linear polarisers, placed in such a way that each row of fibres is covered by a different polariser element (figure 2).

The first row (i.e. the row closest the CXRS fibres) is covered by a linear polariser with a 90° axis, the second row by a polariser with a 0° axis, the third one by a polariser with a 135° and the fourth by the overlap of the 135° polariser and a quarter-wave plate (QWP), where the angles are defined with respect to the fibre array axis. Four vertically arranged LOSs form a group, with group 1 being the innermost group (i.e. the closest to the plasma axis) and group 13 the outermost. The linear polarisers have a width of about 1 mm and the QWP of 0.3 mm. Due to the limited space at our disposal, only a low order crystal QWP could be installed, resulting in a wavelength dependence of the retardation κ, with $\kappa = 2\pi/N(\lambda)$, $N(653\text{ nm}) = 3.7$ and $N(660\text{ nm}) = 4.8$. The MSE lines of sight collect the emission of the interaction between plasma and the atoms accelerated by two neutral beam injectors (NBI), called source 7 (S7) and source 8 (S8). A sketch is shown in figure 3. The LOSs intersect the neutral beams, accelerated at 55 kev, with an angle of about 69 ° almost parallel to the magnetic field (about 6 °), with S8 being slightly more tangential than S7 and thus yielding a stronger Doppler shift. Originally, the optical head was designed such that the LOSs of the same group measure on the same flux surface, as can be seen in figure 4(a), where the dots indicate the positions defined by the points of closest approach between the LOSs and the beam axis. Each colour corresponds to a different polariser. However, it was found during the last experimental campaign (OP2.3, February–May 2025) the optical head to be misaligned with respect to the designed position, leading to a different slightly different measurement position, assessed by Bayesian Inference of the CXRS beam emission spectroscopy (BES) [11] (see figure 4(b)). For this work we will use the latter for the modelling, in order to validate it with the experimental data. Due to hardware limitation, only 11 groups instead of 13 have been used. In total 44 fibres, one for each polariser element, are arranged vertically in front of the spectrometer slit (60 μm width). The spectrometer consists of a commercial NIKON collimating lens (focal length $f_L = 300$ mm,$f/2.8$), a diffraction grating (2160 g mm^{-1}, 130×150 mm^2 ruled area) and a NIKON imaging lens (focal length $f_L = 200$ mm,$f/2.$). A sCMOS camera (pco.edge 5.5 [12], 2560×2160 pixels, pixel area of 6.5×6.5 μm^2, quantum efficiency at the wavelenght of interest around 55%) is placed at the exit image. For the geometry used (angle of incidence 21° and angle of diffraction 71°), the spectrometer has a wavelength range covering 652 nm to 663 nm and a wavelength resolution of 0.13 nm, calculated by measuring the FWHM of the emission peak of a Neon lamp at 659.892 nm. The presented MSE system

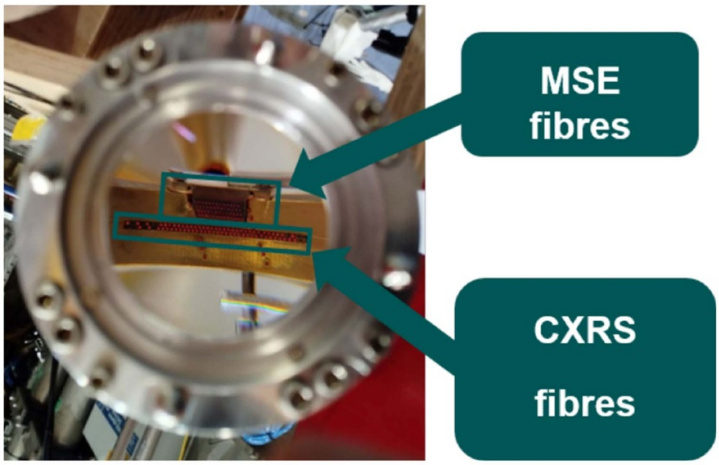

Figure 1. Photo of the MSE and CXRS optical heads.

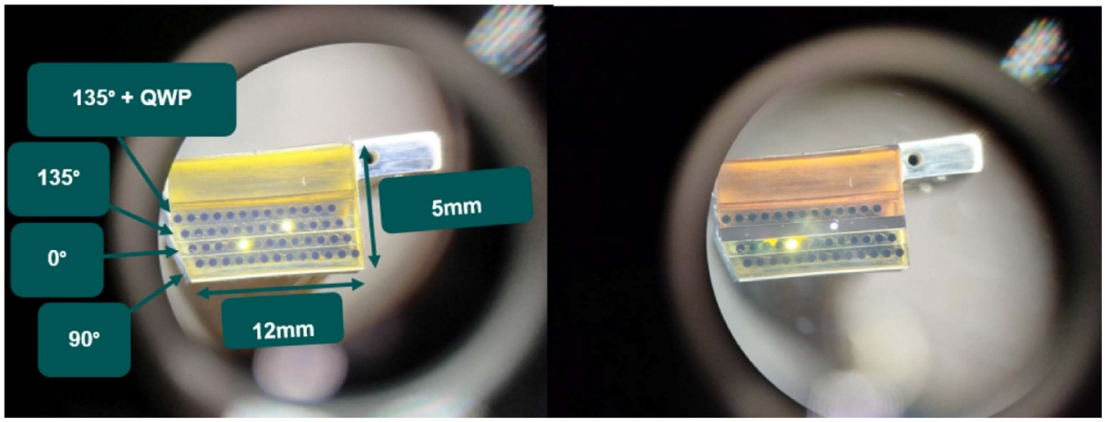

Figure 2. Photo of polarisers and quarter waveplate installed onto the MSE head. The photo on the right was taken placing a polariser foil between the observer and the optical head, in order to highlight the polariser width. It is also possible to notice that the polariser does not cover the light cone of fibres belonging to different rows.

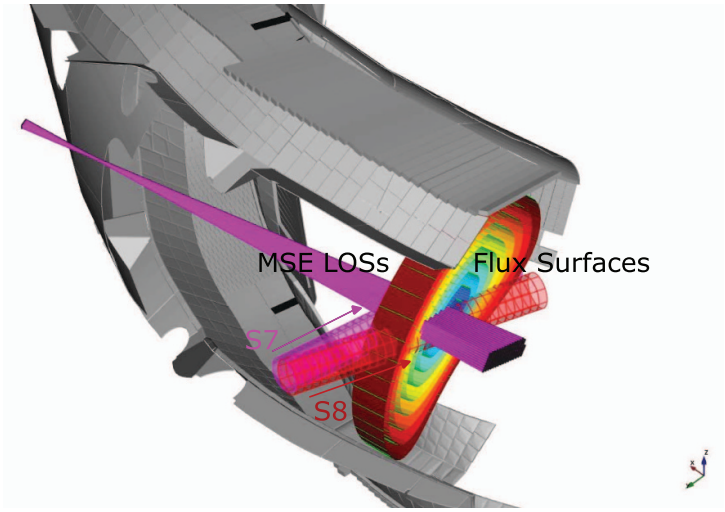

Figure 3. Sketch showing the MSE lines of sight and the intersection with the S7 (purple) and S8 (red) neutral beams.

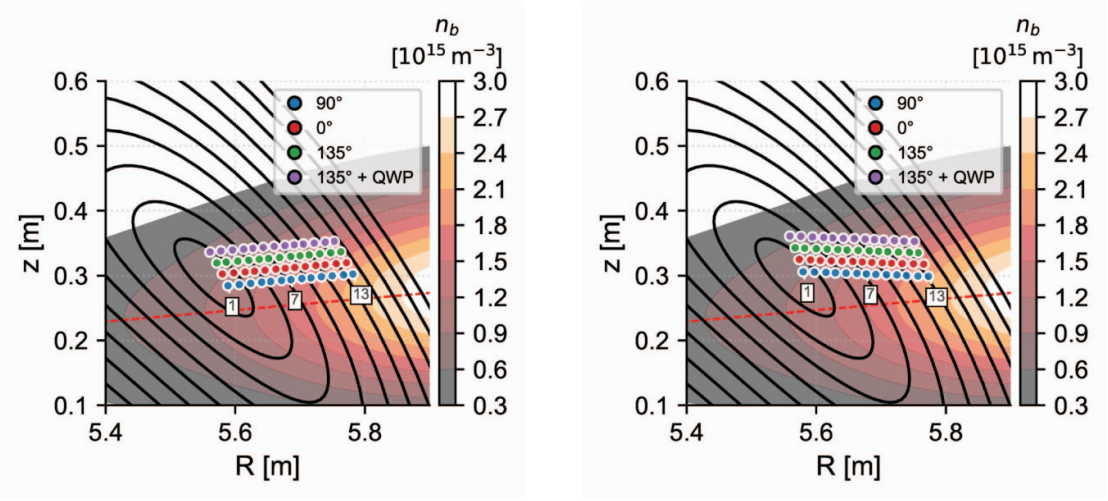

Figure 4. Position of the closest point between the lines of sight and the neutral beam (the shaded area represents the neutral beam density, whereas the dashed line the beam axis of beam 8 with respect to the flux surfaces. (a) As designed lines of sight; (b) position determined with Bayesian inference. Each colour corresponds to a different polariser. Four LOSs with different polarisers constitute a fibre group. Relevant groups for this work (1, 7, 13) are indicated in the plot. The beam density is calculated using the forward model described in [11].

represents an upgrade with respect to a previously installed prototype (focal length $f_L = 750\,\text{mm}$, $f/6.4$, grating 2400 g mm^{-1} with a ruled area of $110 \times 100\,\text{mm}^2$, fibres with $200\,\mu$m diameter). The first prototype, described in [9], was characterised by a low signal-to-ratio, due to the low light throughput. The more suited components, as well as newer equipment manufactured with higher precision standard than for the prototype, was seen to improve the light photon flux by roughly 70 times.

3. Stokes vectors notation

In this work we will express emission polarisation in terms of Stokes vectors $S = [S_0, S_1, S_2, S_3]$, composed of four parameters. Considering the polarisation ellipse, the Stokes vectors can be written as:

$$\mathbf{S} = \begin{pmatrix} S_0 \\ S_1 \\ S_2 \\ S_3 \end{pmatrix} = I \begin{pmatrix} 1 \\ \cos(2\gamma)\cos(2\theta) \\ \sin(2\gamma)\cos(2\theta) \\ \sin(2\theta) \end{pmatrix}. \tag{1}$$

S_0 represents the intensity of polarised and unpolarised light I. S_1 and S_2 describe the linear polarisation and direction and S_3 the circular polarisation, giving γ and θ the orientation of the major axis of the polarisation ellipse with respect to the horizontal axis and shape of the polarisation ellipse, respectively. In contrast to a polarimetry MSE, a 'spectrum' MSE relies on several intensity measurements with linear polarisers [13, 14] in order to reconstruct the Stokes parameters. The measured Stokes parameters S_i^m (indicated by the apex m) of the incident light on the optical head can be written as:

$$S_0^m = I_0 + I_{90} = I_{45} + I_{135} \tag{2}$$

$$S_1^m = I_0 - I_{90} \tag{3}$$

and

$$S_2^m = I_{45} - I_{135} = I_0 + I_{90} - 2I_{135} \tag{4}$$

$$S_3^m = (2I_{\text{QWP}} - S_0^m + S_2^m \; cos\; \kappa(\lambda))\,/sin\; \kappa(\lambda) \tag{5}$$

where I_α is the intensity measured from a fibre LOS with a linear polariser with axis α, I_{QWP} the intensity measured with the QWP and the polariser at 135° and $\kappa = 2\pi/N(\lambda)$ is the phase delay introduced by the QWP as a function of wavelength. Concerning the measurements at W7-X, the emitted polarisation is influenced by the presence of the special aluminium alloy RSA-905 mirror(described by the Müller matrix **M**), therefore the polarisation of the measured light is expected to differ from the polarisation of the emitted light. Considering that:

$$S^m = \mathbf{M} \cdot S \tag{6}$$

one can invert the relation and retrieve the Stokes vector of the emitted light

$$S = \mathbf{M}^{-1} \cdot S^m. \tag{7}$$

The mirror characterisation follows the same procedure as described in section 3.1 of [9]. Finally, knowing the mirror matrix components, the polarisation angle of the emitted light can be taken as the ratio S_2/S_1 (equation (1)) and calculated as:

$$\gamma = 0.5 \tan\left(\frac{S_2}{S_1}\right) = 0.5 \tan\left(\frac{\sum_{i=0}^{3} M_{i2}^{-1} S_i^m}{\sum_{i=0}^{3} M_{i1}^{-1} S_i^m}\right) \tag{8}$$

4. Polarisation measurements and polarisation angle

Four intensity measurements, obtained with different linear polarisers and a QWP are used to reconstruct the polarisation angle. The position of the four lines of sight belonging to the same group was set in such a way to intersect the beam at the same flux surfaces, therefore on isobaric plasma regions. The expected positions of the lines of sight with respect to the flux surfaces are shown in figure 4(b), where the closest points between each LOS and the beam axis are plotted. As shown in section 5, the mapping from Cartesian to flux coordinates depends strongly on the magnetic equilibrium. For each fibre group, we use the major radius R of the 90° polariser fibre LOS as a proxy for the radial coordinate. The Doppler shifted spectra are given by an overlap of several components: for every energy component (55 keV, 55/2 keV, 55/3 keV, with a particle fraction of 0.5, 0.37, 0.13, respectively) the Stark effects split the emission into three components (σ, $\pi-$, $\pi+$) each composed of three transitions (π_2,π_3,π_4 and σ_0 and σ_1), for a total of 27 components. An additional splitting is given by the Zeeman effect, which is however negligible with respect to the Stark effect. In fact, considering a beam energy of 55 keV and an angle $\alpha \approx 55°$ between the beam direction and the magnetic field lines, the ratio between the energy splitting due to the Zeeman effect (ΔE_Z) and the MSE (ΔE_{St}) can be written as:

$$\frac{\Delta E_Z}{\Delta E_{\mathrm{St}}} = \frac{\mu_B}{e a_0 n^2 v \sin(\alpha)}, \tag{9}$$

where μ_B, a_0, e, and v denote the Bohr magneton, the Bohr radius, the elementary charge, and the beam velocity, respectively. For the principal quantum numbers $n = 2$ and $n = 3$, the ratio $\frac{\Delta E_Z}{\Delta E_{\mathrm{St}}}$ is approximately 0.09 and 0.04, respectively. The intensity of the radial electric E_r [15] is about three orders of magnitude smaller than the Lorenz electric field generated by the interaction between the plasma and will be neglected for this work. Additional contributions to the spectra are given by the cold $H\alpha$ emission (656.28 nm), by Halo emission and carbon lines (657.5 nm, 658 nm) and fast ion emission. The latter is expected to contribute to the signal in the spectral region of the $\pi+$ to less than 1% [16] and cancels out when calculating the Stokes components as for equations (2)–(5). Finally, the MSE LOSs intersects two NBIs, therefore the measured spectra is given by the overlap of two beam-emitted spectra. The Stark components as a function of the wavelength are plotted in figure 5. The Stark split is calculated using the equation below:

$$\lambda_{ij} = \frac{1}{1/\lambda_{D,j} + \Delta E_i} \tag{10}$$

where the subscript i denotes the atomic transition, ΔE_i the corresponding energy shift (taken from [17], Chapter 17, table 17.3), j labels the individual energy component and $\lambda_{D,j}$ represents the wavelength of the Doppler-shifted component. It is possible to observe that only the π_2+,π_3+,π_4+ and σ_1

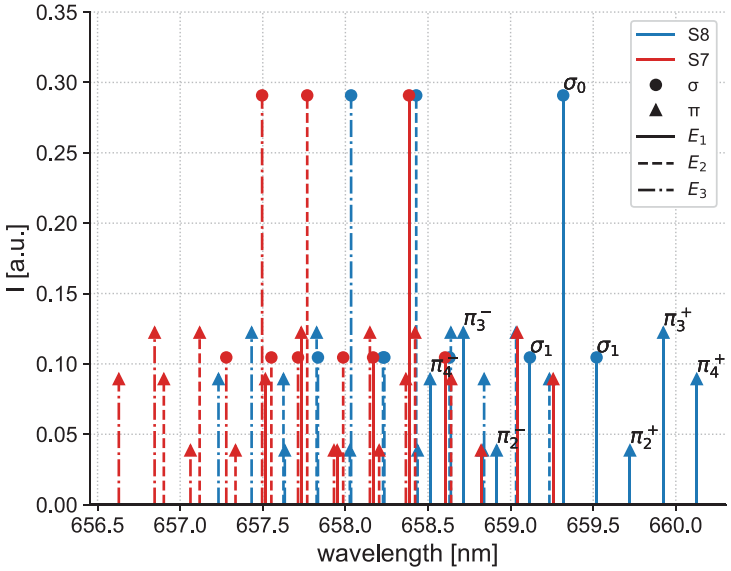

Figure 5. Expected Stark-split components for group 7. In red and blue the components given by the S7 and S8 beams, respectively. The π are indicated by triangles and the σ by circles. The contributions given by the first, second and third energy components are represented by solid, dashed and dot-dashed lines, respectively. The relative intensities refer to the transition probabilities. The beam attenuation and the plasma density have not been taken into account.

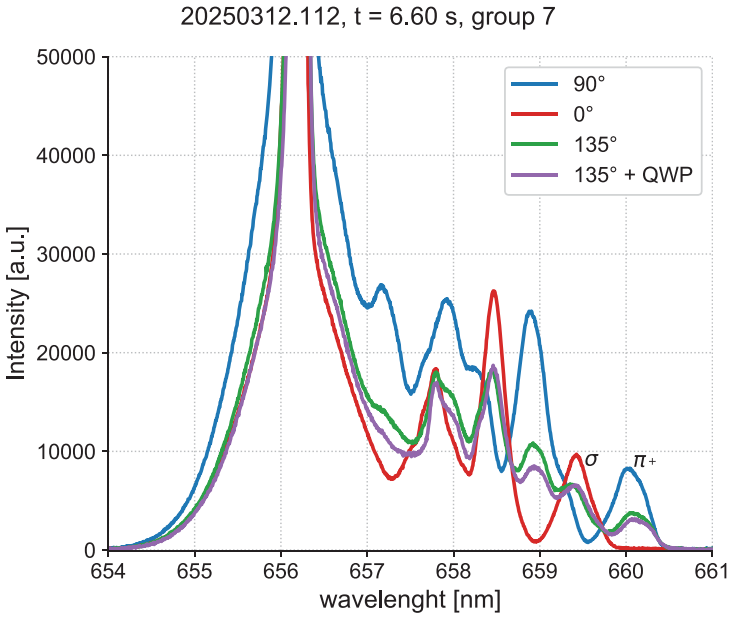

Figure 6. Example of the typical spectra measured with 90°, 0°, 135° polarisers and a 135° polariser covered by a QWP. All spectra are background subtracted, averaged over 6 frames (90 ms) and measured with fibres belonging to group 7. The plot is obtained by averaging 6 frames with an exposure time of 15 ms.

lines of the first energy component for *S*8 are well separated from the other lines. The component overlap is even stronger for measured spectra, in which the line broadening due to the beam divergence and the broadening given by the instrument function are present. An example of measured spectra of group 7 for a representative experiment (20250312.112), which will be introduced more in details in section 6, is given in figure 6, where different colours correspond to spectra measured with different polarising elements. The overlap of different components has a direct effect on the amount of polarisation information it is possible to retrieve from the measurements, as displayed in figure 7. In this figure the Stokes components as function of the wavelength of the emitted light (equations (7) and (8)), are displayed in the second plot. By defining the polarisation degree of the beam emitted radiation as $p = \sqrt{S_1^2 + S_2^2 + S_3^2}/S_0$, it is possible to observe that the spectra exhibit clear ($p > 0.9$) polarised components only for the whole $\pi+$ and parts of the σ and $\pi-$ of the first energy components. For this reason we

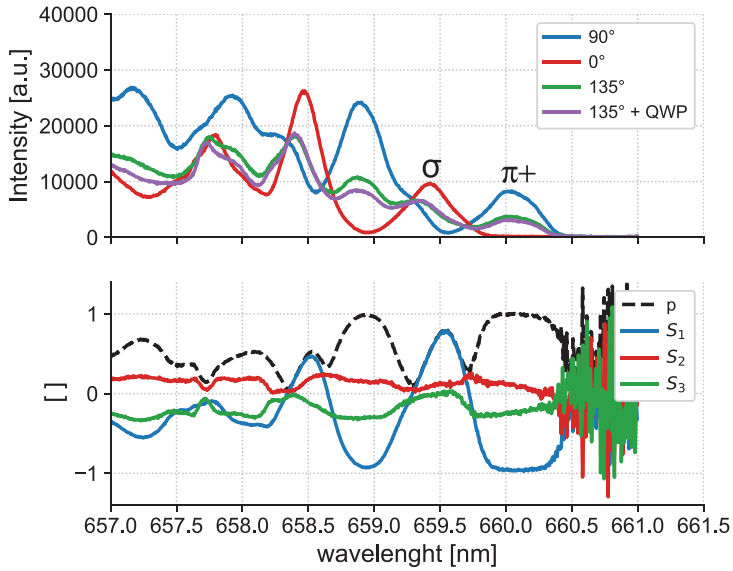

Figure 7. Top plot: BES spectra measured with different polarisers. Bottom plot: polarisation degree (black dashed line) and Stokes components of the BES as a function of the wavelength. The plot is obtained averaging 6 frames with an exposure time of 15 ms.

focus the analysis of this work on the $\pi+$ intensity measurements, being well separated from the other components. An enlargement of the spectral region is provided in figure 8. In this figure the measured data are plotted in red and fit results in blue. The $\pi+$ are fitted with three Gaussian curves (dashed green lines), representing three transitions, and, for the $0°, 135°, 135° + \text{QWP}$, the tail of the neighbouring σ was added as a single Gaussian curve. The distance between the π_2 and π_3 (and between the π_2 and π_4) was constrained to be around 0.20 ± 0.02 nm, consistent with the Stark splitting at W7-X, whereas the initial guess for the ratio between the transitions was set to $\pi_2/\pi_3 = 0.32$ and $\pi_4/\pi_3 = 0.73$, corresponding to the values expected for a statistical population, however the values are allowed to range between 0.1 and 0.4 for the first and 0.5 and 0.95 for the latter, in order to include possible deviations due to non-statistical populations [18, 19]. Additionally the same ratios were constrained for lines of sight belonging to the same fibre group. Within a same group, the peak centre positions were found to differ between different lines of sight. Since a small deviation was also found in other parts of the spectra, likely caused by a slightly different Doppler shift between the lines and wavelength calibration uncertainty, the spectra are shifted in such a way for the position of the π_3+ peaks to coincide. Finally from the measured intensities I_0, I_{90}, I_{135}, I_{QWP} the polarisation angle γ as for equation (8) is calculated, as shown in the top plot of figure 9. For future implementation of the MSE at W7-X it is foreseen to measure the changes of γ with respect to a reference measurement (generally the first available MSE measurement of the experiment, black curve in the top plot) since in a stellarator the flux surfaces exist in vacuum and in such a way it is possible to neglect offsets introduced by the Faraday rotation in the optical elements. An example of $\delta\gamma = \gamma - \gamma_{\text{ref}}$ is shown in the bottom plot of figure 9. For the analysis shown in the rest of the paper, we take the γ values calculated from the fitted curves in figure 8 and average over a wavelength interval 0.15 mm interval around the maximum value of the $\pi+$, in order to use for the analysis the $\delta\gamma$ portion of the spectra with the smallest noise and to avoid overlap with the σ peak tail. Uncertainties using a Monte Carlo approach: the fit parameters are sampled from their covariance matrix, and for each sample the full analysis, from the fits to the calculation of γ is recomputed. The error bars correspond to the standard deviation of the resulting $\delta\gamma$ values across all Monte Carlo realisations. It should be noted that the $\pi+$ position may shift within the experiment, particularly at higher plasma pressures due to diamagnetic effects. To ensure that $\delta\gamma$ reflects changes in the polarisation angle, we calculate γ over a fixed spectral window relative to the fitted peak. This approach avoids misinterpretation of $\delta\gamma$ as artefacts from subtracting different spectral regions caused by $\pi+$ drift. Additionally, it is inherently assumed that γ is a local measurement but in reality it comes from slightly different locations within the same flux surface, since it is derived from four distinct lines of sight, each intersecting the plasma at different beam height position and sampling different regions. Nevertheless, since the primary objective of this work is to demonstrate the upgraded MSE system's capability to

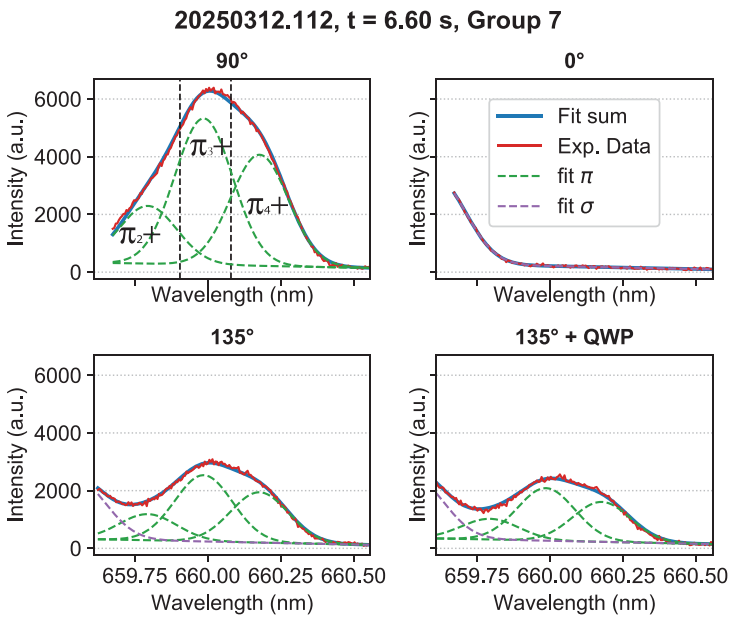

Figure 8. Example of multi Gaussian fits for the $\pi+$ components and σ tail. Each plot highlights the spectral region of the $\pi+$ peak from figure 6 and refers to fibre LOSs with different polarisers. Measured data are displayed in blue and are fitted using a multi Gaussian fit. Each Gaussian component is shown in dashed green curves for the π lines and in purple for the σ tail. The sum is plotted in red.

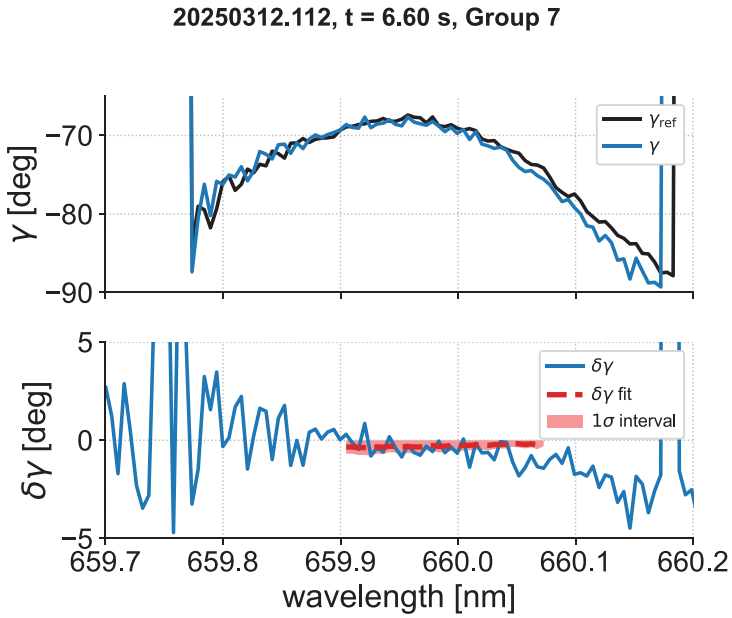

Figure 9. Top plot: γ and γ_{ref} profiles as a function of the wavelength. The spectral range is restricted to the $\pi+$ component. Bottom plot: relative changes of $\delta\gamma$. In blue the $\delta\gamma$ for the measured data, in red from fitting the $\pi+$ components and the standard deviation across all Monte Carlo realisations.

detect changes in the measured signals in response to varying plasma parameters, while maintaining agreement with the theoretical model, this spatial averaging does not compromise the validity of the results, since the modelling is also performed using the real LOSs geometry.

5. Modelling

The model used in this work consists of a modified version of the BES forward model [20], which was successfully used for inferring beam, optical system and plasma parameters (electron density and ion temperature profile) from active H-alpha spectroscopy measurements. The beam attenuation and the

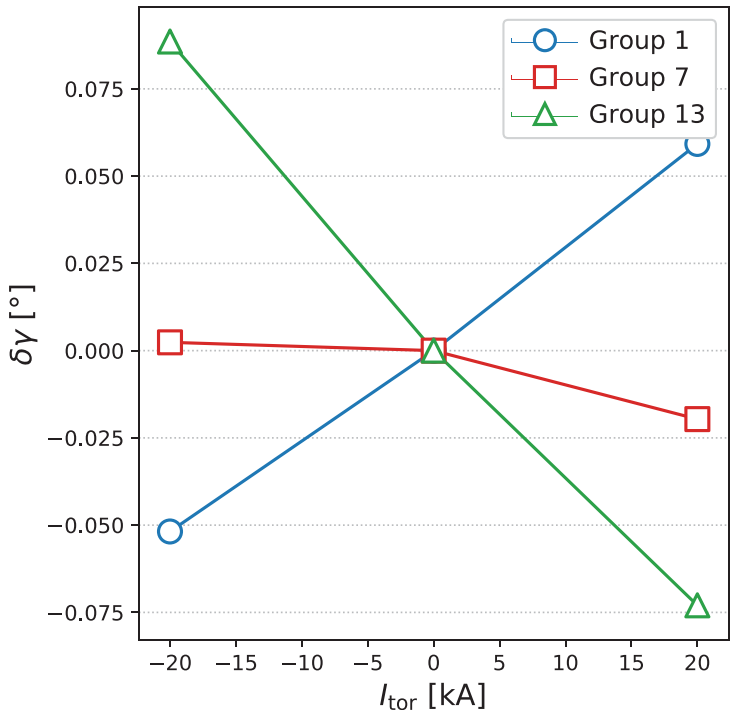

Figure 10. Polarisation angle as a function of the toroidal current. The relative changes are calculated with respect to the equilibrium with $I_{tor} = 0$ kA.

halo formation was implemented in the forward model, in which each source is described as the sum of several Gaussian pencil (Gausscil) beams. For each Gausscil the attenuation and emission due to the interaction with the plasma is calculated solving a step wise collisional radiative model along the beam axis. The halo formation and its H-α emission are computed by solving a coupled, collisional radiative charge exchange (CX) diffusion equation with the beam–plasma CX reaction rate being the initial source term. A detailed description of the model and its verification can be found in [11]. A modified version, which takes into account the MSE lines of sight (LOS) geometry, the linear polarisers and the QWP is employed to calculate the spectra of the beam emission. The spectra are obtained using a VMEC [21] equilibrium and electron temperature, ion temperature and density profiles as inputs. Finally, the polarisation angle γ is calculated from the relation between the spectra corresponding to different polarisers, using the formalism used in section 3 (equations (2)–(5) and (8)). Let us start by considering the polarisation angle changes induced by a finite toroidal current. Three different toroidal current values, representing the full range of typical currents expected for present operational parameter, (−20 kA, 0 kA, 20 kA) were used to create the VMEC equilibria and, for the sake of simplicity, we considered flat plasma pressure profile $p(r) = 0$ Pa and a flat current density profile. The results are plotted in figure 10, in which $\delta\gamma$ is plotted as a function of I_{tor} for three fibre groups, where $\delta\gamma = \gamma - \gamma_{ref}$ (figure 9) and γ_{ref} corresponds to the case $I_{tor} = 0$ kA. We observe that for a change of 20 kA, a change of less than 0.1° is expected. Importantly, $\delta\gamma$ is expected to be larger for experiments with localised currents (e.g. ECCD). Nevertheless, figure 10 confirms the expected order of magnitude, which approaches the current experimental sensitivity limit. We also investigated the effects of different pressure profiles on the polarisation angle (while keeping $j_{tor} = 0$). The profiles used to calculate the magnetic equilibrium with VMEC are plotted in figure 11(a) as a function of the effective radius, along with the positions of the fibre groups. Notably, due to the Shafranov shift, the fibre position relative to the effective radius changes as the pressure increase and the innermost groups shift from the inboard side to the outboard side. The dependence of $\delta\gamma$ as a function of $\langle\beta\rangle$ is depicted in figure 11(b). For all considered fibre groups, $\delta\gamma$ varies up to 5° and presents a non-monotonic trend, which can be also explained by the fact that, as shown in figure 11(a), the relative measurement positions change within the $\langle\beta\rangle$ scan. A conservative estimate of the model accuracy was obtained by varying the plasma pressure within a range of 10%, consistent with the experimental uncertainty. Such variations were found to induce changes in $\delta\gamma$ of the order of 0.1°–0.2°, depending on the fibre group, which can be considered as the accuracy limit of our model. In contrast to the I_{tor} scan, $\delta\gamma$ is expected to give changes that can be experimentally detected with the MSE diagnostic and a validation of the model is shown in the next section. Improvement in the BES

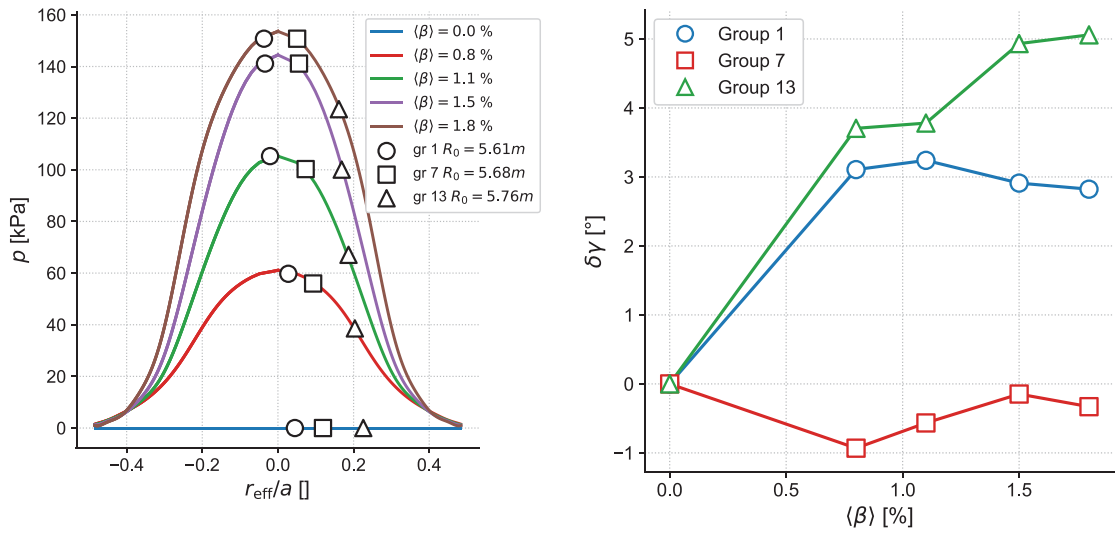

Figure 11. (a) Mapping of three selected fibre groups for different pressure profiles. The solid lines represent the pressure profiles as a function of the effective radius. Negative and positive radii values correspond to the inboard and outboard side, respectively. The white shapes show the radial position of three selected fibre groups. (b) Modelled polarisation angle γ calculated by the model as a function of the plasma pressure for selected fibre groups. All data are offset relative to the vacuum ($\beta = 0$) values.

model are foreseen, for instance, by including the radial electric field and the Zeeman effect, which are neglected here since they are expected to result in changes significantly smaller than the $\delta\gamma$ measured in this work. These corrections will be incorporated in future versions of this work. Regarding the Zeeman effect, the possible polarisation contribution still needs to be taken into account; however it is not expected to play a relevant role for the data presented in this work, since the focus is on relative changes of γ. A comparison between model results and experimental data is discussed in the next section.

6. Experimental data

We present in this section $\delta\gamma$ measurements and comparison with the above introduced model. As discussed in the previous section, the present toroidal currents are too small to be measured as the typical values for I_{tor}/B at W7-X are about $5\,\mathrm{kA\,T^{-1}}$, whereas for a stellarator of comparable size, such as the Large Helical Device (LHD) [14] the typical values lie between $50–70\,\mathrm{kA\,T^{-1}}$, thus leading to changes in γ on the order of 1°, at least a order of magnitude higher than the expected values at W7-X. Therefore, we focus in this chapter on a so-called 'high performance' experiment [22, 23], featuring high core β, and therefore a relatively strong Shafranov shift. An overview of the relevant parameters for experiment *20250312.112* is depicted in figure 12, whereas selected pressure profiles are shown in figure 13. A pure electron cyclotron resonance heating (ECRH) phase with pellet injection is present for the first 5.65 s of the experiment, after which NBI is operated for 4 s (top panel) and the ECRH power is raised from 2 to 4 MW. This phase is characterised by an increase in diamagnetic energy (middle panel) and ion temperature, reaching its maximum at around 6.5 s, followed by a relatively stable phase. The evolution of γ is shown in the bottom panel, in which significant changes are measured, especially between $t = 5.65$ and $t = 6.6$ s, in which W_{dia} increases by a factor of three. In fact a β change, for which W_{dia} is taken as a proxy, will result in changes in $|\mathbf{B}|$ due to the plasma diamagnetism and a change in the intensity of the Pfirsch–Schlüter currents, which, by creating a vertical component of $\mathbf{B}$ is expected to change the pitch angle, and therefore the polarisation angle γ. Additional contributions, which are however expected to be negligible in a first approximation (see discussion in section 5), are given by the toroidal currents such as the neutral beam current drive (NBCD) and the bootstrap current and the radial electric field. Whereas the most external fibre group shows a monotonic trend, which stabilises between $t = 6.5$ s and $t = 10$ s, groups 3 and 7 are characterised by a non-monotonic trend, in which γ decreases for the first 0.5 s and then increases again. We emphasise again that the relative position of the fibre groups with respect to the flux surfaces strongly changes due to the Shafranov shift, therefore a proper mapping to r_{eff} needs to be included in future works. Finally, the measured $\delta\gamma(t) = \gamma(t) - \gamma(t_0)$ is compared with predictions given by our model for selected times, where $\gamma(t_0)$ corresponds to the value of the first available measurement ($t_0 = 5.65\,\mathrm{s}$). For each time step of interest, a VMEC equilibrium is calculated from

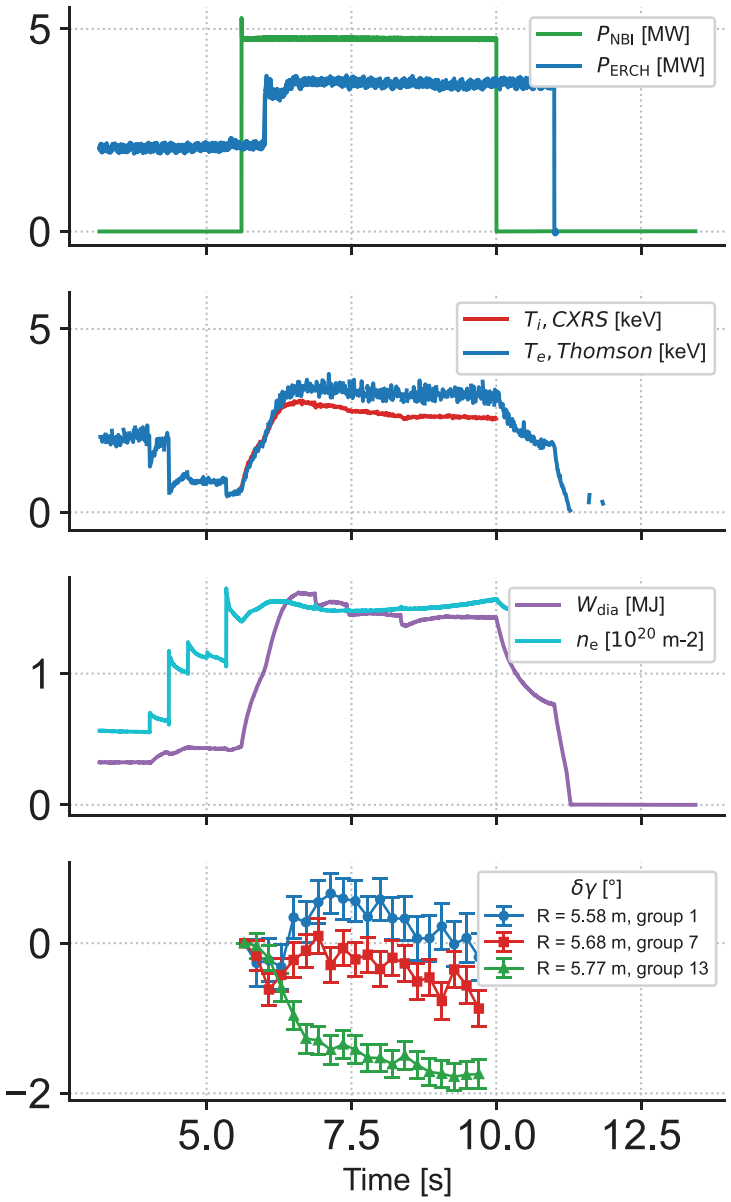

Figure 12. Selected plasma parameters for experiment *20250312.112*. First panel: NBI and ERCH heating power. Second panel: core electron and ion temperature .Third panel: diamagnetic energy. Fourth panel: evolution of $\delta\gamma$ for selected fibre groups. Data are taken by averaging 6 frames, each with an exposure time of 15 ms.

the plasma pressure $p = k_B(T_e\ n_e + T_i\ n_e/Z_{eff})$(figure 13), where k_B is the Boltzmann constant, T_e and n_e the electron temperature and density, obtained by the Thomson Scattering diagnostic [24], respectively, T_i is the ion temperature measured by the CXRS diagnostic [10] and $Z_{eff} \approx 1.2$ the effective atomic number. The comparison between the temporal evolution of the relative polarisation angle obtained from the model ($\delta\gamma_{model}$) and from the experimental data ($\delta\gamma_{exp}$) is plotted in figure 14 for three fibre groups, spanning from the core to mid-plasma and showing that the modelled data (solid red line) generally agree within the error (1σ) bars with the experimental data (black dots). Notably the model follows the same trend as the experimental data and as for figure 12, we also observe in figures 14(a) and (b) an initial decrease in γ. In figure 14(c) it is possible to observe a good match between the first and the last points, whereas the model shows a larger $\delta\gamma$ between the $t = 6$ s and $t = 7$ s, which corresponds to the phase of strong W_{dia} increase.

Despite the fact that for each fibre group the 4 LOSs do not intersect the beam in the same position, but rather on the same flux surface, the good agreement with the model confirms the diagnostic capabilities of the MSE at W7-X. The match between the modelled and experimental data is the first

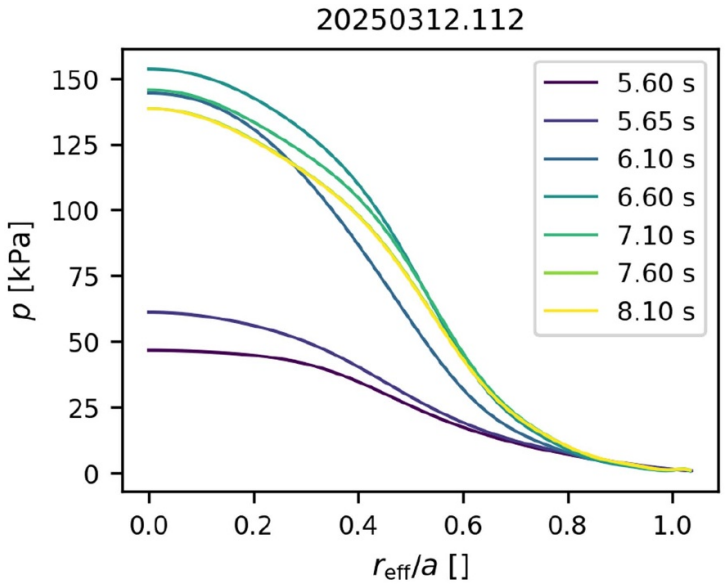

Figure 13. Plasma pressure profiles at different instants. The profiles are used as a input for VMEC to calculate a corresponding equilibrium.

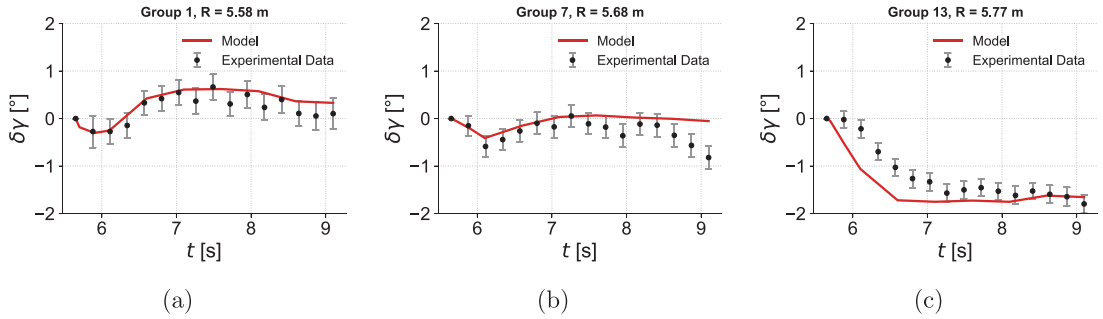

Figure 14. Comparison between the polarisation angles $\delta\gamma$ obtained by the experimental data (black dots) and the model (solid red line) for the innermost, middle and outermost MSE fibre groups.

step toward the assessment of the Lorentz field and therefore the magnetic field pitch angle and the rotational transform. Since the dependence of the measured polarisation on the plasma parameters (beta, Shafranov shift etc) is very complex, inference of these from the measured data requires advanced analysis tools, e.g. using the described forward model in a Bayesian inference framework [25].

7. Summary and discussion

In this work we discussed the results obtained with an improved MSE system. A new spectrometer, with new optical fibres and a new optical head was installed, resulting in an increase in the SNR from 10 to around 80. The overlap of the several energy components results in a limited wavelength region with a defined polarisation, namely the region in which the $\pi+$ can be identified, therefore the polarisation analysis was limited to this well-separated component. The polarisation angle was obtained using four intensity measurements (3 linear polarisers and a linear polariser with a quarter wave-plate) and was compared to the evolution of toroidal current and plasma pressure in a selected experiment. Even if the SNR was highly improved, no clear measurements of the toroidal current was available, mainly due to small currents present at W7-X (about 10 kA), which are orders of magnitude smaller than currents in machines of comparable size, such as LHD [14]. Significant changes in γ were instead detected for experiments with large β changes. A comparison between experimental and modelled data show a good

agreement in $\delta\gamma$ indicating the reliability of our emission model to measure changes of the plasma pressure. At present, the toroidal current assessment seems out of reach and would require further improvement of the SNR. The possibility however to use the MSE diagnostic, in particular when integrated in a Bayesian framework with the CXRS system [11] might offer the possibility to constraint the plasma pressure, thus yielding an improved equilibrium reconstruction , from which the rotational transform can be obtained. Future improvements of the model such as by including Faraday rotation, E_r and Zeeman effect are ongoing, in order to improve the $\delta\gamma$ estimation even further.

Acknowledgment

This work has been carried out within the framework of the EUROfusion Consortium, funded by the European Union via the Euratom Research and Training Programme (Grant Agreement No 101052200 — EUROfusion). Views and opinions expressed are however those of the author(s) only and do not necessarily reflect those of the European Union or the European Commission. Neither the European Union nor the European Commission can be held responsible for them.

Data availability statement

The data cannot be made publicly available upon publication because they are not available in a format that is sufficiently accessible or reusable by other researchers. The data that support the findings of this study are available upon reasonable request from the authors.

ORCID iDs

M Zanini 0000-0002-8717-1106
O Ford 0000-0002-5646-4758
S Bannmann 0000-0003-0772-9278
E V Hausten 0009-0001-4298-4891
P Zs Poloskei 0000-0001-7781-5599
K Rahbarnia 0000-0002-5550-1801
T Romba 0000-0002-2727-9385
R C Wolf 0000-0002-2606-5289

References

[1] Wolf R *et al* 2017 *Nucl. Fusion* **57** 102020
[2] Grieger G 1989 Summary on technology and reactor concepts, including safety and environmental aspects *Plasma Physics and Controlled Nuclear Fusion Research III* (*Nice, France*) pp 631–43
[3] Beidler C D *et al* 2021 *Nature* **596** 221–6
[4] Fisch N J and Boozer A H 1980 *Phys. Rev. Lett.* **45** 720–2
[5] von Goeler S, Stodiek W and Sauthoff N 1974 *Phys. Rev. Lett.* **33** 1201–3
[6] Zanini M *et al* 2020 *Nucl. Fusion* **60** 106021
[7] Levinton F M, Fonck R J, Gammel G M, Kaita R, Kugel H W, Powell E T and Roberts D W 1989 *Phys. Rev. Lett.* **63** 2060–3
[8] Wolf R, Bock A, Ford O, Reimer R, Burckhart A, Dinklage A, Hobirk J, Howard J, Reich M and Stober J 2015 *J. Instrum.* **10** 10008
[9] Zanini M *et al* 2024 *J. Instrum.* **19** 12010
[10] Ford O P *et al* 2020 *Rev. Sci. Instrum.* **91** 023507
[11] Bannmann S *et al* 2024 *Plasma Phys. Control. Fusion* **66** 065001
[12] (available at: https://www.excelitas.com/product-category/)
[13] Voslamber D 1995 *Rev. Sci. Instrum.* **66** 2892–903
[14] Ida K Yoshinuma M, Suzuki C, Kobuchi T and Watanabe K Y 2010 *Fusion Sci. Technol.* **58** 383–93
[15] Pablant N, Langenberg A, Alonso A, Baldzuhn J, Beidler C, Bozhenkov S, Burhenn R, Brunner K, Dinklage A and Fuchert G E A 2020 *Nucl. Fusion* **60** 036021
[16] Poloskei P Z, Geiger B, Jansen van Vuuren A, Äkäslompolo S, Ford O, Spanier A, Neelis T, McNeely P and Hartmann D (W7-X-Team) 2023 *Nucl. Fusion* **64** 026008
[17] Condon E U and Shortley G H 1935 *The Theory of Atomic Spectra* 8th edn (Cambridge University Press)
[18] Mandl W, Wolf R C, Hellermann M G V and Summers H P 1993 *Plasma Phys. Control. Fusion* **35** 1373–94
[19] Marchuk O, Ralchenko Y, Janev R K, Biel W, Delabie E and Urnov A M 2009 *J. Phys. B: At. Mol. Opt. Phys.* **43** 011002
[20] Bannmann S *et al* 2023 *J. Instrum.* **18** 10029
[21] Hirshman S P and Whitson J 1983 *Phys. Fluids* **26** 3553

[22] Ford O et al 2024 Nucl. Fusion 64 086067
[23] Bozhenkov S et al 2026 Plasma Phys. Controlled Fusion 68 055015
[24] Bozhenkov S et al 2017 J. Instrum. 12 10004
[25] Svensson J and Werner A 2007 Large scale Bayesian data analysis for nuclear fusion experiments 2007 IEEE Int. Symp. on Intelligent Signal Processing pp 1–6
[26] Grulke O et al 2024 Nucl. Fusion 64 112002